Aalborg Universitet

AALBORG UNIVERSITY
DENMARK

Voltage Stability and Transient Symmetrical Fault Current Control of Voltage-Controlled MMCs

Li, Yingbiao; Guo, Jianbo; Wu, Heng; Wang, Xiongfei

Publication date:
2020

Document Version
Accepted author manuscript, peer reviewed version

Link to publication from Aalborg University

Voltage Stability and Transient Symmetrical Fault Current Control of Voltage-Controlled MMCs

Yingbiao Li, Jianbo Guo, *Senior Member, IEEE*, Heng Wu, *Student Member, IEEE*, Xiongfei Wang, *Senior Member, IEEE*, Bing Zhao, Shanshan Wang, Guanglu Wu

Abstract—**This paper presents a design-oriented analysis on the voltage stability and the transient fault current limitation of voltage-controlled modular multilevel converter (MMC) with L-filters. First, a dual-loop voltage control based on the L-filter plant is systematically designed, where the upper limits of controller parameters for ensuring the small-signal stability are identified. Then, considering the transient current limitation during faults, the lower boundaries of inner current controller parameters are derived. Within the region of allowed controller parameters, the optimization is further made to minimize the closed-loop output impedance of MMC, which enhances the output voltage stiffness against the load current disturbance. Lastly, time-domain simulations corroborate the theoretical analysis.**

Keywords—Modular Multilevel Converter (MMC), voltage control, controller design, fault current

NOMENCLATURE

P_w, Q_w	Active power and reactive power of wind farm
u_w, i_w	Voltage and current of grid connection point of wind farm
Z_w	Impedance of the transmission line
u_s	Voltage of PCC of MMC
u_c, i_s	Voltage output by MMC and current input into MMC
u_g	Voltage of the location of the fault
u_α, u_β,	Voltage in two-phase stationary frame
i_α, i_β	Current in two-phase stationary frame
i_{dc}, u_{dc}	DC current and DC voltage of MMC
L_{eq}, R_{eq}	Equivalent inductance and resistance of MMC
L_g	Equivalent inductance from fault point to PCC of MMC
f_c, ω_c	Crossover frequency and angular frequency
ω_0	Resonant frequency of PR controller
u_s^*, i_s^*	Reference value of voltage and current.
I_{smax}^*	Maximum value of the current limiter
$T_{abc2\alpha\beta}$	Clarke transformation
G_d, T_d	Time delay and time constant
H_u, T_{d1}	Filter of voltage feedforward and time constant
G_i, G_v	Transfer function of inner current loop regulator and outer voltage loop regulator.
K_{pi}, K_{ii}	Proportional gain and resonant gain of inner current loop regulator
K_{pv}, K_{iv}	Proportional gain and resonant gain of outer voltage loop regulator
$\delta_1\%$, t_s	Overshoot and convergence time

I. INTRODUCTION

THE modular multilevel converter (MMC) high voltage direct-current (HVDC) transmission systems have recently drawn increasing attentions in the grid integration of large-scale wind farms. Compared with the line-commutated converters (LCC)-HVDC, the MMC-HVDC is expected to have better dynamic performance when feeding to weak [1], [2] or passive [3], [4] ac power networks. On the wind farm side, the MMC needs to operate as a voltage source, forming the system voltage and frequency. Consequently, both the high-performance ac voltage control and the fast overcurrent limiting capability during ac faults become critical [5], [6]. Moreover, due to the versatile nature of wind, the load current of the voltage-controlled MMC can be fluctuated, and thus the output voltage of the MMC needs to be stiff against the load current disturbances.

The controller parameters have a significant impact on the stability and transient performance of MMCs. Designing the voltage controller for voltage-source converters (VSCs) has been thoroughly discussed, considering the phase margin (PM), the gain margin (GM) and the steady-state error [7], [8]. Yet, those studies are mainly based on the LC-filtered VSCs, where the dual voltage-current control loops can be readily designed based on the second-order LC-filter plant [9]. In contrast, only the L-filter is used with MMCs, and hence no LC-filter resonance needs to be considered when designing the voltage controller [10], [11]. Further, differing from the capacitor voltage of the LC-filtered VSCs, the PCC voltage of the MMC cannot be treated as a state variable, due to the lack of capacitance. Therefore, the controller design for the LC-filtered VSCs cannot be directly extended to MMCs.

The single-loop voltage control is implemented with the MMC in [12], yet the fault current of the MMC cannot be limited in this case, when there is a short circuit fault in the ac side of voltage-controlled MMC. Considering the limited overcurrent capability of MMCs [13], [14], a fast fault current control is important. To limit the fault current, fault current limiters are employed in [6], [15], [16]. In practice, the dual-loop control that consists of the outer voltage loop and the inner current loop is generally used for the fault current control

[15], [17]. However, in those works, the transient fault current is always assumed to be equal to the limit value of the current limiter [18], [19]. The parametric effect of current controller on the transient fault current is often overlooked. Since the limit value is merely a steady-state value of the fault current, the fault current can be much higher than the limit during the transient process, which affects the safe operation of MMC.

The reliable operation of wind farms depends on a stable voltage formed by the MMC station. The small-signal stability of voltage-controlled MMC has been explored in [20], [21], but what is not yet clear is the impact of parameters on the stiffness of MMC output voltage under the power fluctuations of wind farms. In [22], the voltage stiffness is improved when a severe fault occurs by adjusting the reactive power output of the voltage-controlled MMC. To address the large power and voltage disturbances, the voltage stiffness is enhanced by an additional frequency control loop [6]. However, the effects of the inner current regulator and outer voltage regulator on the voltage stiffness of the MMC are not addressed.

The voltage feedforward control is commonly used in the control of grid-connected VSCs [23] and MMCs [24]. The grid impedance is introduced to the control system through the feedforward loop and the influence of voltage feedforward on the voltage stability of grid-connected converters is studied in [25], [26], [27]. It can be seen that voltage feedforward has an important impact on the control and operation characteristic of converter. However, when the MMC is connected with wind farms, u_s is formed by MMC, while the effects of voltage feedforward on the stiffness of the voltage and fault current limitation of the MMC need to be clarified.

This paper thus presents a systematic controller design guideline for the dual-loop voltage-controlled MMC-HVDC. The proportional-resonant (PR) regulators are used in both the outer voltage and inner current loops. Considering the effect of the voltage feedforward, the upper limits of controller parameters are identified first based on the small-signal model and stability analysis of the dual-loop voltage control. Then, the parametric effects of the current controller on the current overshoot and settling time are analyzed, which yields the lower limits of current controller parameters. Next, within the region of permitted controller parameters, the optimization is further made to minimize the closed-loop output impedance of MMC, in order to enhance the voltage stiffness against the power flucations from the wind farms. Lastly, time-domain simulations validate the effectiveness of the design guideline.

II. PARAMETERS DESIGN BASED ON THE STABILITY REQUIREMENT

A. System Description

Fig. 1 illustrates the single-line diagram of the MMC with the dual-loop voltage control system implemented in the stationary frame. It is noted that the stationary-frame PR controller can be mathematically derived from the P-Integral (PI) controller in the synchronous (dq-) reference frame [28], [29]. The purpose of selecting the stationary-frame is to control both the positive- and negative-sequence components, and meanwhile avoid using the sequence decomposition algorithm and Park transformations. Thus, the phase variation
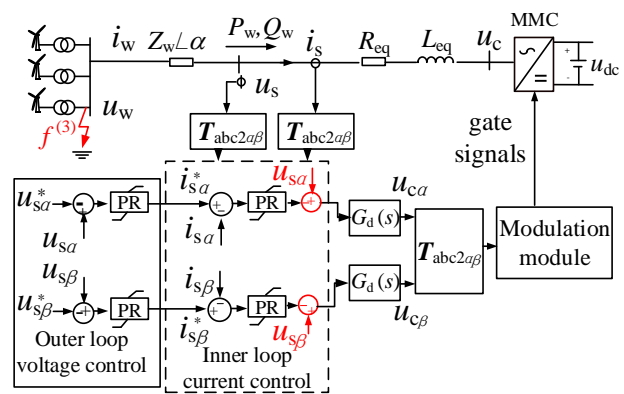

Fig. 1 Single-line diagram of MMC with dual-loop voltage control system.
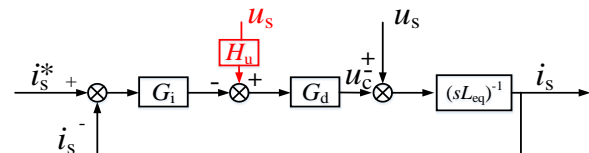

Fig. 2. Transfer function diagram of inner current loop.
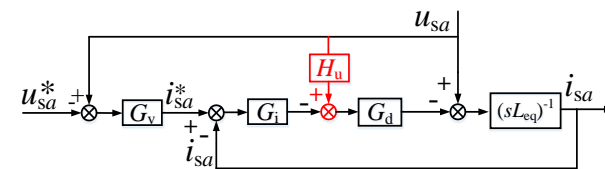

Fig. 3. Transfer function diagram of V-F controlled MMC.

of PCC voltage, which may affect the dynamics of the dq-frame control [28], can be avoided in the stationary frame.

In Fig. 1, u_s denotes the voltage at the point of common connection (PCC), u_c is the output voltage of MMC, i_s is the current injected into MMC, L_{eq} is the equivalent inductance, and "*" represents the reference of the current and voltage. A constant dc-link voltage of the MMC is assumed and the timescale of internal dynamics is well decoupled from the external ac voltage control dynamics. With these assumptions, the MMC power stage can be approximated as a linear time-invariant (LTI) plant [30], [31].

B. Controller Parameters Design of Inner Loop

Fig. 2 shows the control block diagram of the inner current loop, where G_i is the current regulator and G_d represents the time delay. Since the internal control dynamic of MMC has little effect at the crossover frequency of the inner loop f_c, it is not considered in the parameter tuning of dual-loop voltage control [30].

The open-loop transfer function of the inner current loop can be obtained as

$$G(s) = G_i G_d \frac{1}{sL_{eq}} \tag{1}$$

where G_i and G_d are expressed as

$$\begin{cases} G_i = K_{pi} + \dfrac{K_{ii}s}{s^2 + \omega_0^2} \\ G_d = e^{-sT_d} \end{cases} \tag{2}$$

K_{pi} is proportional coefficient, K_{ii} is resonant gain of inner current loop regulator, and T_d is time constant of time delay.

Assuming that the crossover frequency $\omega_c \gg \omega_0$, G_i can be approximated as

$$G_i\left(\omega_c\right) \approx K_{pi} + \frac{K_{ii}}{j\omega_c} \tag{3}$$

In order to guarantee the system stability, PM > 0 and GM > 0 are required at the crossover frequency. If the proportional gain of the PR regulator is designed to have a dominant effect at the crossover frequency, i.e.,

$$K_{pi} = 10 \cdot \frac{K_{ii}}{2\pi f_c} \tag{4}$$

The loop gain and its phase response can be approximated as (5).

$$L\left(\omega_c\right) \approx 20 \lg \left[\frac{K_{pi}}{\left(2\pi f_c\right) L_{eq}}\right] \tag{5}$$

$$\varphi\left(\omega_c\right) \approx -90° - 57.3 T_d \left(2\pi f_c\right)$$

To ensure PM > 0 and GM > 0, the parameters should be designed as

$$\begin{cases} f_c < \dfrac{90}{104.6\pi T_d} \\ K_{pi} < \left(2\pi f_c\right) L_{eq} \end{cases} \tag{6}$$

If the integral gain of the current regulator is designed to have a dominant effect at the crossover frequency, i.e.,

$$\frac{K_{ii}}{2\pi f_c} = 10 \cdot K_{pi} \tag{7}$$

The loop gain and its phase response can be approximated as (8).

$$L\left(\omega_c\right) \approx 20 \lg \left[\frac{K_{ii}}{2\pi f_c} \cdot \frac{1}{\left(2\pi f_c\right) L_{eq}}\right] \tag{8}$$

$$\varphi\left(\omega_c\right) \approx -180° - 57.3 T_d \left(2\pi f_c\right)$$

From (8), it can be seen that PM is always smaller than 0. Hence, the inner loop controller can't be designed with the integral gain playing a dominant role at f_c, and it can only be designed with the proportional gain dominating at the crossover frequency, where (6) is satisfied.

C. Controller Parameters Design of Outer Loop

In the islanded system, the MMC is controlled as a voltage source forming the u_s. And the influence of voltage feedforward is investigated in this part.

1) With the voltage feedforward loop

The mathematical model of outer voltage loop control can be obtained as (9).

$$\begin{cases} i_{s\alpha}^* = G_v \cdot (u_{s\alpha} - u_{s\alpha}^*) \\ i_{s\beta}^* = G_v \cdot (u_{s\beta} - u_{s\beta}^*) \end{cases} \tag{9}$$

where

$$G_v = K_{pv} + \frac{K_{iv}s}{s^2 + \omega_0^2} \tag{10}$$

Combining (9) with Fig. 2, the block diagram of the outer loop and the inner loop in the $\alpha\beta$ frame is shown as Fig. 3, where H_u represents the filter of the voltage feedforward, i.e.,

$$H_u = \frac{1}{1 + sT_{d1}} \tag{11}$$

From Fig. 3, the transfer function can be obtained as

$$u_{s\alpha} = \frac{G_i G_V G_d}{1 + G_i G_V G_d - G_d H_u} u_{s\alpha}^* + \frac{G_i G_d + sL_{eq}}{1 + G_i G_V G_d - G_d H_u} i_{s\alpha} \tag{12}$$

Then, the open-loop transfer function is expressed as

$$G_{c1}\left(s\right) = G_i G_V G_d - H_u G_d \tag{13}$$

If the proportional gain of the PR voltage regulator is designed to have a dominant effect at the crossover frequency of the voltage loop, i.e.,

$$K_{pv} = 10 \cdot \frac{K_{iv}}{2\pi f_c} \tag{14}$$

Then, the amplitude-frequency characteristic and phase-frequency characteristics can be approximated as (18), which is shown in the bottom of this page.

From (6) and (18), to ensure the PM > 0 and GM > 0, the satisfactory region can be obtained as

$$K_{pi} K_{pv} \leq 1 \tag{15}$$

If the integral gain of the PR regulator is designed to have a dominant effect at the crossover frequency, i.e.,

$$\frac{K_{iv}}{2\pi f_c} = 10 \cdot K_{pv} \tag{16}$$

Then, the amplitude-frequency characteristic at crossover frequency can be approximated as

$$L\left(\omega_c\right) \approx 20 \lg \sqrt{1 + 2\frac{K_{pi} K_{iv} T_{d1}}{1 + \left(\omega_c T_{d1}\right)^2} + \left(\frac{K_{pi} K_{iv}}{\omega_c}\right)^2} \tag{17}$$

From (17), the GM is always smaller than 0.

Therefore, the outer voltage loop regulator can only be designed with the proportional gain dominated at the crossover frequency, in which (15) must be satisfied.

$$\begin{cases} L\left(\omega_c\right) \approx 20 \lg \left| K_{pi} K_{pv} - \dfrac{1}{1 + j\omega_c T_{d1}} \right| \\ \varphi\left(\omega_c\right) \approx \begin{cases} \arctan \dfrac{\omega_c T_{d1}}{K_{pi} K_{pv} \left[1 + \left(\omega_c T_{d1}\right)^2\right] - 1} - 57.3\omega_c T_d & \left(K_{pi} K_{pv} \geq \dfrac{1}{1 + \left(\omega_c T_{d1}\right)^2}\right) \\ 180° - 57.3\omega_c T_d + \arctan \dfrac{\omega_c T_{d1}}{K_{pi} K_{pv} \left[1 + \left(\omega_c T_{d1}\right)^2\right] - 1} & \left(K_{pi} K_{pv} < \dfrac{1}{1 + \left(\omega_c T_{d1}\right)^2}\right) \end{cases} \end{cases} \tag{18}$$
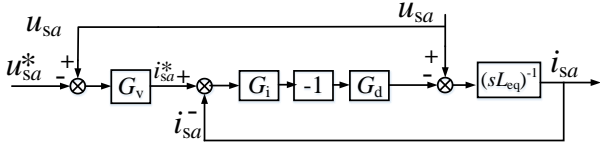
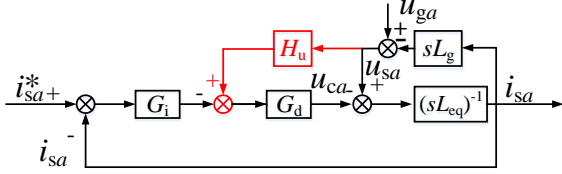Fig. 4 Transfer function diagram without voltage feedforward loop.

Fig. 5 Transfer function diagram of inner current loop after fault.

2) *Without the voltage feedforward loop*

If there is no voltage feedforward loop, the control block diagram is changed as shown in Fig. 4, from which, the closed-loop transfer function can be derived as

$$u_{s\alpha} = \frac{G_i G_V G_d}{1 + G_i G_V G_d} u_{s\alpha}^* + \frac{G_i G_d + s L_{eq}}{1 + G_i G_V G_d} i_{s\alpha} \qquad (19)$$

Then, the open-loop transfer function is obtained as

$$G_{c1}(s) = G_i G_V G_d \qquad (20)$$

Substituting (2) and (10) into (20), if the proportional gain of the PR regulator is designed to have a dominant effect at the crossover frequency, the amplitude-frequency and phase-frequency characteristics at the crossover frequency can be obtained as

$$\begin{cases} L(\omega_c) \approx 20 \lg |K_{pi} K_{pv}| \\ \varphi(\omega_c) \approx -114.6 T_d \pi f_c \end{cases} \qquad (21)$$

When $K_{pi} K_{pv} < 1$, the $L(\omega_c)$ is always below 0. Therefore, the satisfactory region can be obtained as

$$K_{pi} K_{pv} < 1 \qquad (22)$$

If the integral gain of the PR regulator is designed to have a dominant effect at the crossover frequency, the amplitude-frequency and phase-frequency response at the crossover frequency can be obtained as

$$L(\omega_c) \approx 20 \lg \frac{K_{pi} K_{iv}}{\omega_c} \qquad (23)$$

$$\varphi(\omega_c) \approx -90° - 114.6 T_d \pi f_c$$

To ensure the PM > 0, the parameters should be designed as

$$\begin{cases} K_{pi} K_{iv} \leq \omega_c \\ 114.6 T_d \pi f_c \leq 90° \end{cases} \qquad (24)$$

Hence, without using the voltage feedforward loop, the parameters of the outer voltage regulator can be designed with either the proportional gain or the integral gain dominating at the crossover frequency. When the proportional gain is designed to have a dominant effect at the crossover frequency, (22) must be satisfied. When the integral gain is designed to have a dominant effect at the crossover frequency, (24) needs to be satisfied.

III. PARAMETERS DESIGN BASED ON THE FAULT CURRENT LIMITATION

Short-circuit faults in the ac system increasingly arise as the power scale of wind farm is enlarged. Due to the limited overcurrent capability of the MMC, the fault current control is critical, and the fault current overshoot needs to be effectively suppressed. In this work, only the symmetrical three-phase short circuit fault at the ac-side of the MMC is considered.

A. *With the voltage feedforward loop*

Fig. 5 shows the control block diagram of the inner current loop after the short circuit fault on the ac side. $u_{g\alpha}$ is the voltage of the location of the fault, L_g is the equivalent fault inductance.

Based on Fig. 5, the transfer function of the inner current loop can be obtained as

$$i_{s\alpha} = \frac{G_i G_d}{s(L_{eq} + L_g - L_g H_u G_d) + G_i G_d} i_{s\alpha}^* \\ + \frac{1 - G_d H_u}{s(L_{eq} + L_g - L_g H_u G_d) + G_i G_d} u_{g\alpha} \qquad (25)$$

Considering a severe three-phase short-circuit fault, the voltage amplitude at the fault location reduces to zero. The reference current amplitude reaches the maximum of the limiter. Since the control system is a linear system, $i_{s\alpha}$ is the superposition of the two step responses, which are

$$\begin{cases} G_{i_{ref\_step}} = \frac{G_i G_d}{s(L_{eq} + L_g - L_g G_d) + G_i G_d} \\ G_{u_g\_step} = \frac{1 - G_d}{s(L_{eq} + L_g - L_g G_d) + G_i G_d} \end{cases} \qquad (26)$$

Without loss of generality, the analysis is carried out at the initial current of 0 and the initial phase of 0 degree of $u_{g\alpha}$. According to the characteristic of PR controller, the phase of reference current is opposite to the voltage of $u_{g\alpha}$ after the fault. Thus, the reference current and voltage can be given by

$$\begin{cases} i_{s\alpha}^* = -I_{s\alpha max}^* \cos(\omega t) u(t) \\ u_{g\alpha} = |u_{g\alpha}| \cos(\omega t) [u(t + t_0) - u(t)] \end{cases} \qquad (27)$$

where $I_{s\alpha max}^*$ is the maximum of the limiter.

With the Laplace transformation, (25) can be transformed as

$$i_{s\alpha}(s) = -I_{s\alpha max}^* \frac{s}{s^2 + \omega_0^2} G_{i_{ref\_step}} \\ + (e^{st_0} - 1) |u_{g\alpha}| \frac{s}{s^2 + \omega_0^2} G_{u_g\_step} \qquad (28) \\ = G_1 - e^{st_0} G_2 + G_2$$

Considering that

$$L^{-1}(e^{st_0} G_2) = u(t + t_0) f_2(t + t_0) \qquad (29)$$

which has little effect on the $i_{s\alpha}(t)$ at time $t = 0$, and thus it can be ignored. Then, (28) can be approximated as

$$i_{s\alpha}(s) = i_{s\alpha}^*(s)G_{i_{ref}\_step} + G_{u_g\_step}u_{g\alpha}(s)$$

$$= \frac{1}{s}G_{i\_step} + \frac{1}{s}G_{u\_step} \qquad (30)$$

$$= \frac{1}{s}G_{step}$$

where

$$\begin{cases} G_{i\_step} = \dfrac{-s^2}{s^2+\omega_0^2}I_{s\alpha max}^* G_{i_{ref}\_step} \\[2mm] G_{u\_step} = -|u_{g\alpha}|\dfrac{s^2}{s^2+\omega_0^2}G_{u_g\_step} \\[2mm] G_{step} = G_{i\_step} + G_{u\_step} \end{cases} \qquad (31)$$

The time-domain current response can then be obtained as

$$i_{s\alpha}(t) = L^{-1}(\frac{1}{s}G_{step}) \qquad (32)$$

The amplitude changes of current and voltage can be equivalent to the step response of G_{step}, where the overshoot and convergence time can be obtained. Since the order of G_{step} is too high to express $i_{s\alpha}(t)$ analytically, it is directly calculated through the MATLAB, and the parametric effect of the inner current regulator and the time delay on the overshoot are illustrated in Fig. 6.

It is seen that the parametric effect on the overshoot has a minimum value when $K_{pi} = K_{pi1}$ with a certain value of T_d. When $K_{pi} < K_{pi1}$, the larger the K_{pi}, the smaller the overshoot of fault current is obtained. In contrast, when $K_{pi} > K_{pi1}$, the larger the K_{pi}, the larger the overshoot of fault current is seen. From Fig. 6 (b), it is seen that the effect of T_d on the overshoot has a minimum value when $T_d = T_{d0}$. When $T_d < T_{d0}$, the larger T_d, the smaller the fault current overshoot is. When $T_d > T_{d0}$, the larger T_d, the larger the fault current overshoot is. In order to ensure that the system has sufficient damping, the K_{pi} has a minimum K_{pimin}, and T_d has a maximum T_{dmax}.

Considering that the allowed overshoot is $\delta_1\%$, the satisfactory region of K_{pi} can be obtained as

$$\max(K_{pi\,min}, K_{pi\_\delta_1\%\,min}) \le K_{pi} \le K_{pi\_\delta_1\%\,max} \qquad (33)$$

where $K_{pi\_\delta_1\%\,min}$ and $K_{pi\_\delta_1\%\,max}$ are calculated with (32) with the condition of $\delta_1\%$.

The parametric effect of the inner current regulator and the time delay on the convergence time are shown as Fig. 7. From Fig. 7 it can be seen that the larger the K_{pi} and the smaller the T_d, the shorter the convergence time t_s is obtained. Assuming that the allowed convergence time is t_{s1}, the satisfactory region can be obtained as

$$K_{pi\_t_{s1max}} \le K_{pi} \qquad (34)$$

where $K_{pi\_t_{s1max}}$ is calculated through with (32) in the condition of t_{s1}.

Considering that the initial phase of the voltage is φ_1, (27) can be written as

$$\begin{cases} i_{s\alpha}^* = -I_{s\alpha max}^* \cos(\omega t + \varphi_1)u(t) \\ u_{g\alpha} = |u_{g\alpha}|\cos(\omega t + \varphi_1)\big[u(t+t_0)-u(t)\big] \end{cases} \qquad (35)$$
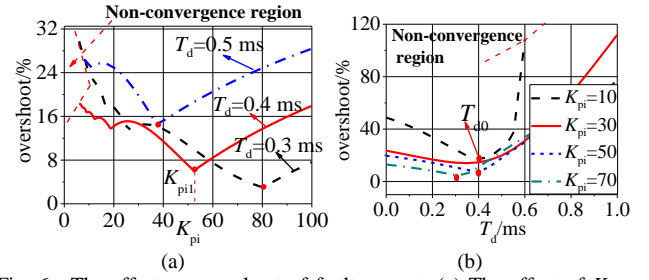
And (31) should be modified as (36).

Fig. 6. The effect on overshoot of fault current. (a) The effect of K_{pi} on overshoot. (b) The effect of T_d on overshoot.
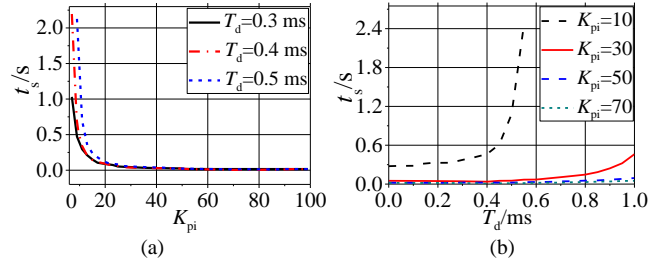

Fig. 7. The effect on convergence time of fault current. (a) The effect of K_{pi} on convergence time. (b) The effect of T_d on convergence time
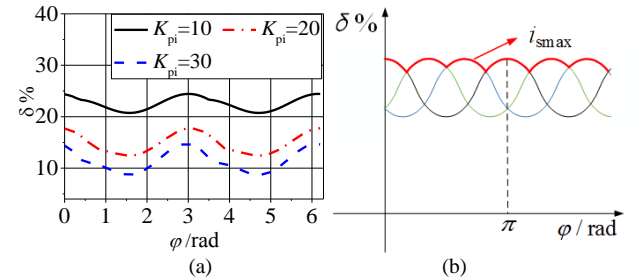

Fig. 8 The effect of initial phase on overshoot. (a) The effect of φ_1 on overshoot of $i_{s\alpha}$ in different K_{pi}. (b) The maximum of fault current of 3-phase
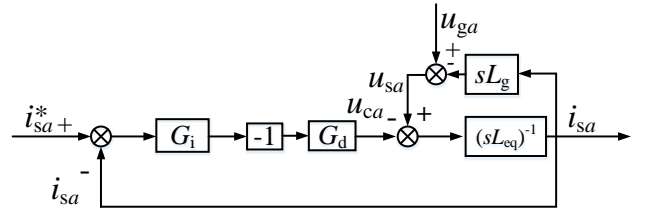

Fig. 9 Transfer function diagram of inner current loop after fault without voltage feedforward.

$$\begin{cases} G_{i\_step} = I_{s\alpha max}^*\left(-\cos\varphi_1\dfrac{s^2}{s^2+\omega_0^2}+\sin\varphi_1\dfrac{314s}{s^2+\omega_0^2}\right)G_{i_{ref}\_step} \\[3mm] G_{u\_step} = -|u_{g\alpha}|\left(\cos\varphi_1\dfrac{s^2}{s^2+\omega_0^2}-\sin\varphi_1\dfrac{314s}{s^2+\omega_0^2}\right)G_{u_g\_step} \\[3mm] G_{step} = G_{i\_step} + G_{u\_step} \end{cases} \qquad (36)$$

The effect of φ_1 on the overshoot is shown as Fig. 8. From Fig. 8 (a), it can be seen that the overshoot of α is related with the initial phase. Thus, the overshoot is largest when the fault occurs at the phase of $n*\pi/3$ (n = 0, 1, 2, 3…), and the overshoot is smallest when the fault occurs at the phase of $(2n+1)*\pi/6$ (n = 0, 1, 2, 3…) as shown in Fig. 8 (b). Hence, both the overshoot and the convergence time of fault current should be calculated with $\varphi_1 = 0$, which is the most serious condition, and the satisfactory region can be obtained as (37).

$$\max(K_{pi\,min}, K_{pi\_\delta_1\%\,min}, K_{pi\_t_{s1max}}) \le K_{pi} \le K_{pi\_\delta_1\%\,max} \qquad (37)$$
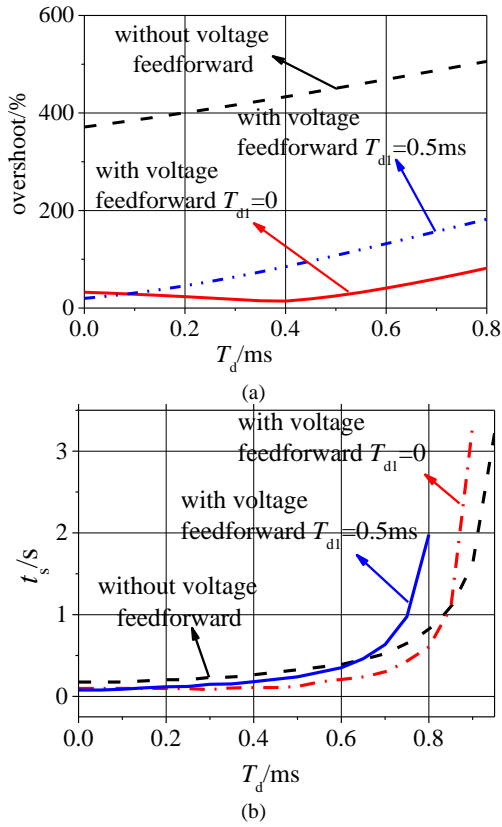
(a)

(b)

Fig. 10 The effect of voltage feedforward on overshoot and convergence time of fault current. (a) The effect of voltage feedforward on overshoot. (b) The effect of voltage feedforward on convergence time
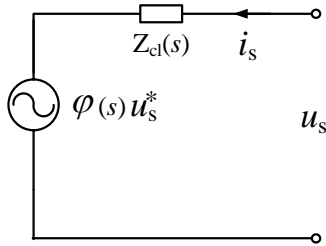

Fig. 11 The equivalent circuit of MMC

B. Without the voltage feedforward loop

When there is no voltage feedforward loop used, the control block diagram of the inner current loop after the short circuit fault is shown as Fig. 9. And the transfer function can be obtained as

$$i_{s\alpha} = \frac{G_i G_d}{s(L_{eq} + L_g) + G_i G_d} i_{s\alpha}^* + \frac{1}{s(L_{eq} + L_g) + G_i G_d} u_{g\alpha} \quad (38)$$

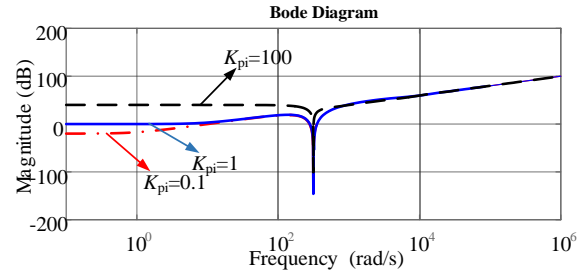Analyzing the overshoot of the fault current in the same

Fig. 12 The amplitude-frequency characteristic of Z_{cl} ($K_{pi}K_{pv} = 1, \omega_c = 4070$)

way, the results are shown in Fig. 10. From Fig. 10 it can be seen that the overshoot of fault current is significantly larger than that with a voltage feedforward yet the convergence time is similar. Hence, the voltage feedforward control is necessary considering the overshoot of fault current.

IV. THE EFFECT ON IMPENDENCE OF PARAMETERS

The equivalent circuit of MMC at the ac side is shown in Fig. 11. Generally, a smaller modulus of closed-loop output impendence can improve the voltage stiffness against the load current variation. Hence, the control parameters are further optimized to reduce the output impendence magnitude.

A. With the voltage feedforward loop

With the voltage feedforward loop used, according to (12), the closed-loop output impendence of MMC is derived as

$$Z_{cl} = \frac{G_i G_d + s L_{eq}}{1 + G_i G_V G_d - H_u G_d} \quad (39)$$

First, at the low frequency, G_d and H_u can be simplified as

$$\begin{cases} G_d \approx 1 \\ H_u \approx 1 \end{cases} \quad (40)$$

Consequently, the impedance modulus can be obtained as (42) shown in the bottom of this page. From (42), it can be seen that the larger the K_{pi} and the smaller the $K_{pi}K_{pv}$, the larger the $|Z_{cl}(\omega)|$ will be obtained.

Second, at the high frequency, G_d and H_u cannot be ignored, where G_d is replaced as (41).

$$e^{-j\omega T_d} = \cos(-\omega T_d) + j\sin(-\omega T_d) \quad (41)$$

The impedance modulus can be obtained as (43), where ωL_{eq} is much larger than others in the numerator of (43) at high frequencies, and consequently K_{pi} has little effect on the impedance modulus.

Fig. 12 plots the amplitude frequency responses of $Z_{cl}(\omega)$ with the different parameters. It is clear that the difference of the impendence modulus is only seen in the low frequency range, which agrees well with the theoretical analysis.

$$\left| Z_{cl}(\omega) \right| = \sqrt{ \frac{ \left(K_{pi}^2 + \left(\omega L_{eq} \right)^2 + \left(K_{pi} \omega \omega_c \right)^2 \big/ 100 \left(-\omega^2 + \omega_0^2 \right)^2 + L_{eq} K_{pi} \omega^2 \omega_c \big/ \left[5\left(-\omega^2 + \omega_0^2 \right) \right] \right) }{ \left(K_{pi} K_{pv} \right)^2 \left[1 + \omega^2 \omega_c^2 \big/ \left[100 \left(-\omega^2 + \omega_0^2 \right)^2 \right] \right]^2 } } \quad (42)$$

$$\left| Z_{cl}(\omega) \right| = \sqrt{ \frac{ K_{pi}^2 - 2\omega L_{eq} K_{pi} \sin(\omega T_d) + \left(\omega L_{eq} \right)^2 }{ 1 + \left(K_{pi} K_{pv} \right)^2 - 2 K_{pi} K_{pv} \dfrac{1 + \cos(-\omega T_d) + \left(\omega T_{d1} \right)^2 \cos(-\omega T_d)}{1 + \left(\omega T_{d1} \right)^2} + \dfrac{1 - 2\left(\cos(-\omega T_d) + \sin(-\omega T_d) \omega T_{d1} \right)}{1 + \left(\omega T_{d1} \right)^2} } } \quad (43)$$
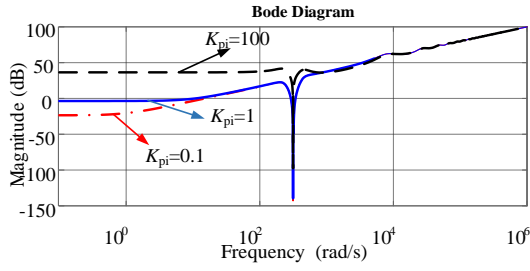
Fig. 13 The amplitude-frequency characteristic of Z_{cl} ($K_{pi}K_{pv} = 0.5, \omega_c = 4070$)
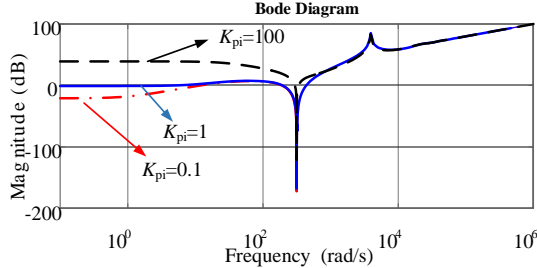

Fig. 14 The amplitude-frequency characteristic of Z_{cl} ($K_{pi}K_{iv} = 4070, \omega_c = 4070$)

B. Without the voltage feedforward loop

When there is no voltage feedforward loop, according to (19), the impendence of MMC can be obtained as

$$Z_{cl} = \frac{G_i G_d + sL_{eq}}{1 + G_i G_V G_d} \quad (44)$$

The parameters of outer voltage loop regulator can be designed with either the proportional gain or the integral gain of the PR regulator dominating at the crossover frequency.

1) Proportional gain dominating at the crossover frequency.

With the proportional gain dominating at the crossover frequency, the impedance modulus at the low frequency range can be obtained as (47) in the bottom of this page, from which, it can be seen that the larger the K_{pi} and the smaller the $K_{pi}K_{pv}$, the larger the $|Z(\omega)|$ is obtained.

At high frequencies, the impedance modulus is obtained as (45).

$$\left| Z_{cl}\left(\omega\right) \right| = \sqrt{\frac{K_{pi}^2 - 2\omega L_{eq} K_{pi} \sin\left(\omega T_d\right) + \left(\omega L_{eq}\right)^2}{\left(K_{pi} K_{pv}\right)^2 + 1 + 2 K_{pi} K_{pv} \cos\left(-\omega T_d\right)}} \quad (45)$$

where the ωL_{eq} is far larger than others, and hence the K_{pi} has little effect on the impedance modulus. Fig. 13 plots the amplitude-frequency responses of $Z_{cl}(\omega)$.

2) Integral gain dominating at the crossover frequency

With the integral gain dominating at the crossover frequency, the impedance modulus in the low frequency range

is expressed as (48), which is shown in the bottom of this page. From (48), the same effect of K_{pi}, and $K_{pi}K_{iv}$ on $|Z(\omega)|$ as that with the proportional gain can be observed.

In the high frequency range, the impedance modulus can be obtained as

$$\left| Z_{cl}\left(j\omega\right) \right| = \sqrt{\frac{K_{pi}^2 + \left(\omega_c L_{eq}\right)^2 - 2\omega_c L_{eq} K_{pi} \sin\left(\omega_c T_d\right)}{1 - 2 K_{pi} K_{iv} / \omega_c \sin\left(\omega T_d\right) + \left(K_{pi} K_{iv} / \omega_c\right)^2}} \quad (46)$$

where similarly the ωL_{eq} is far greater than others, and K_{pi} has little effect on the impedance modulus.

The amplitude-frequency characteristic of $Z_{cl}(\omega)$ is shown in Fig. 14. It is clear that the controller parameters only affect the impedance modulus in the low frequency range.

V. SIMULATIONS

The simulation study is carried out in PSCAD to verify the effectiveness of the parameters design method. The arm-averaged model of the MMC given in Fig. 1 is adopted in the simulation, in which each bridge is replaced by a controlled voltage source [32]. The wind farm is modeled by a controlled current source with the PLL. The parameters used in the simulation are given in Table I.

Fig. 15 shows the parametric impact of the inner current loop on voltage stability with $T_d = 0.3$ ms. Based on (6), it can be calculated that the stability of the inner current loop requires $f_c < 913$ Hz and $K_{pi} < 523.5$. The simulation result with $f_c = 920$ Hz > 913 Hz and $K_{pi} = 577 > 523.5$ is given in Fig. 15 (a), where the unstable operation of the MMC can be clearly observed. In contrast, the MMC can be stabilized when the
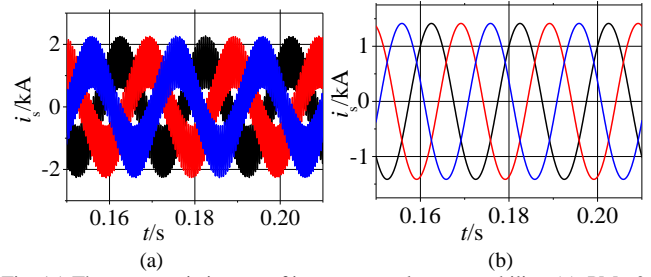

Fig. 15 The parametric impact of inner current loop on stability. (a) PM <0. (b) PM = 10 °

TABLE I
MAIN CIRCUIT PARAMETERS USED IN SIMULATIONS

SYMBOL	DESCRIPTION	VALUE
u_s	Rated ac voltage of MMC	230 kV
P	Rated power of the MMC	400 MW
L_{eq}	Equivalent inductance of MMC	0.1 H
L_W	Line inductance	0.05 H
I_{max}	The limit value of current limiter	1.0 p.u.
f_0	Grid frequency	50 Hz
T_d	Time delay	0.3 ms

$$\left| Z_{cl}\left(\omega\right) \right| = \sqrt{\frac{K_{pi}^2 + \left(\omega L_{eq}\right)^2 + \left(K_{pi}\omega\omega_c\right)^2 / 100\left(-\omega^2 + \omega_0^2\right)^2 + L_{eq} K_{pi} \,\omega^2\omega_c \big/ 5\left(-\omega^2 + \omega_0^2\right)}{\left[1 + 2 K_{pi} K_{pv} - K_{pi} K_{pv}\left(1 + K_{pi} K_{pv}\right)\omega_c^2\omega^2 \big/ 50\left(-\omega^2 + \omega_0^2\right)^2 + \left(K_{pi} K_{pv}\right)^2 \left[1 + \omega^2\omega_c^2 \big/ 100\left(-\omega^2 + \omega_0^2\right)^2\right]\right]^2}} \quad (47)$$

$$\left| Z_{cl}\left(\omega\right) \right| = \sqrt{\frac{K_{pi}^2 + \left(\omega L_{eq}\right)^2 + \left(K_{pi}\omega\omega_c\right)^2 / 100\left(-\omega^2 + \omega_0^2\right)^2 + L_{eq} K_{pi} \,\omega^2\omega_c \big/ 5\left(-\omega^2 + \omega_0^2\right)}{\left[1 + 20 K_{pi} K_{iv} / \omega_c - K_{pi} K_{iv}\omega_c \omega^2 \big/ 5\left(-\omega^2 + \omega_0^2\right)^2 + \left(10 K_{pi} K_{iv} / \omega_c\right)^2 \left[1 + \omega^2\omega_c^2 \big/ 100\left(-\omega^2 + \omega_0^2\right)^2\right]\right]^2}} \quad (48)$$

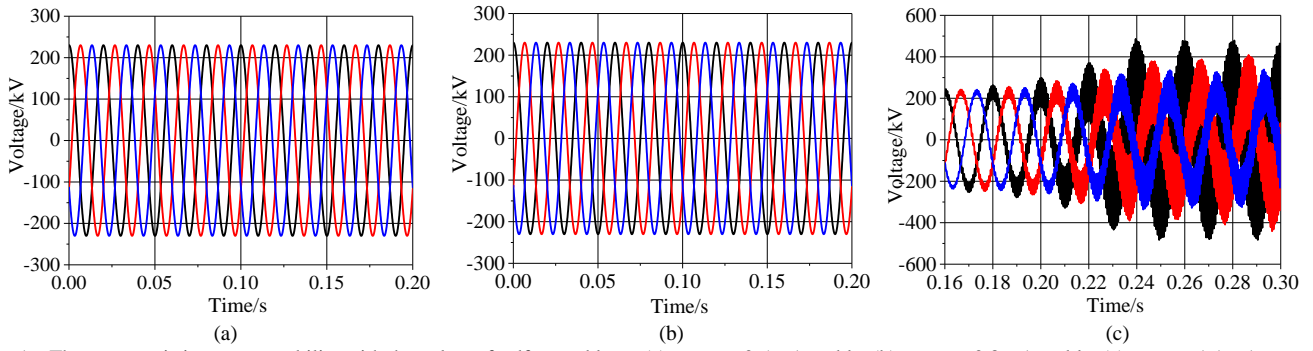Fig. 16 The parametric impact on stability with the voltage feedforward loop. (a) $K_{pi}K_{pv} = 0.5 < 1$, stable. (b) $K_{pi}K_{pv} = 0.8 < 1$, stable. (c) $K_{pi}K_{pv} = 1.1 > 1$, unstale
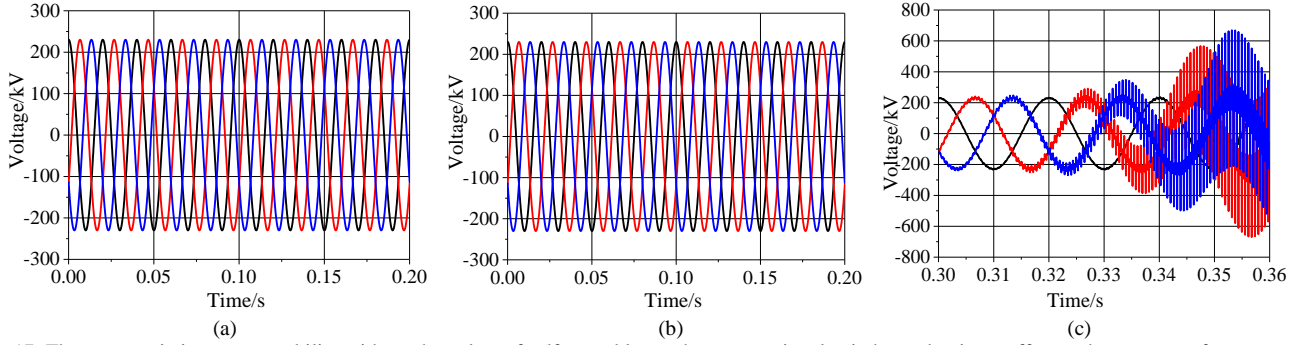

Fig. 17 The parametric impact on stability without the voltage feedforward loop when proportional gain has a dominant effect at the crossover frequency. (a) $K_{pi}K_{pv} = 0.5 < 1$, stable. (b) $K_{pi}K_{pv} = 0.8 < 1$, stable .(c) $K_{pi}K_{pv} = 1.1 > 1$, unstale
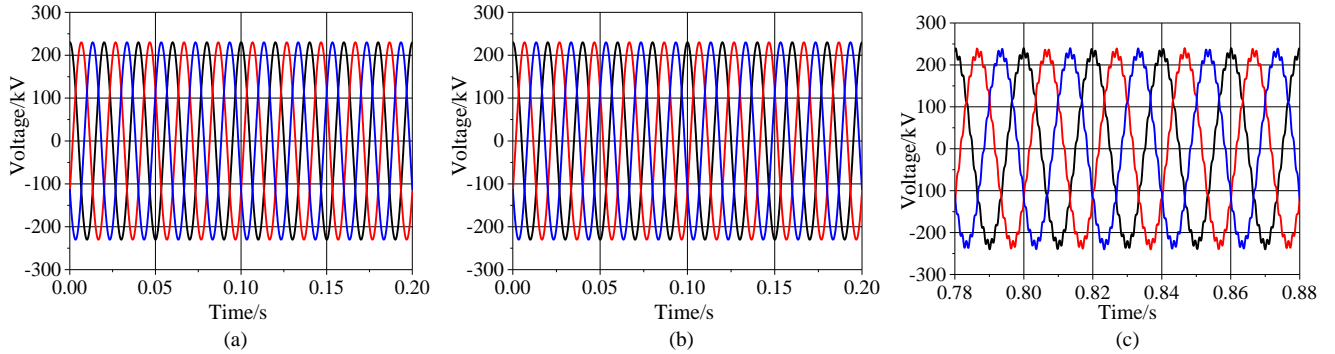

Fig. 18 The parametric impact on stability without the voltage feedforward loop when integral gain has a dominant effect at the crossover frequency. (a) $K_{pi}K_{iv} = 3000 < 4070$, stable. (b) $K_{pi}K_{iv} = 4000 < 4070$, stable. (c) $K_{pi}K_{iv} = 5500 > 4070$, unstable
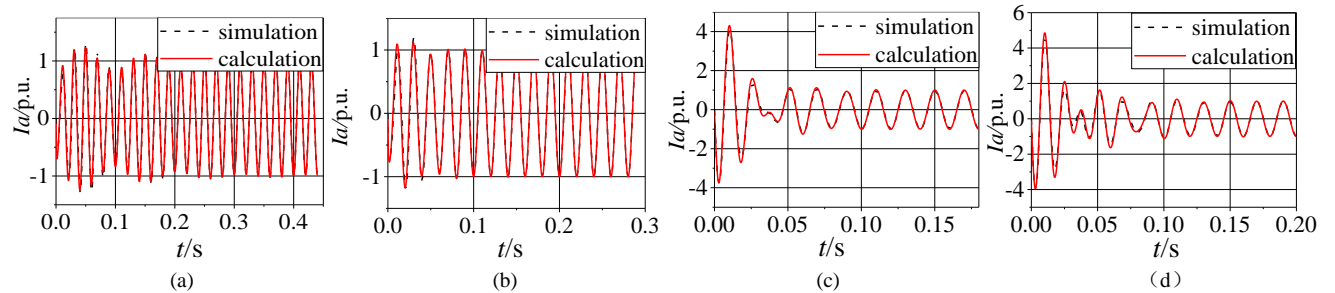

Fig. 19 Comparison of simulation and calculation of the fault current in different parameters. (a) $T_d = 0.3$ ms, $K_{pi} = 10$ with voltage feedforward (b) $T_d = 0.3$ms, $K_{pi} = 20$ with voltage feedforward.（c）$T_d = 0.3$ ms, $K_{pi} = 20$ without the voltage feedforward.（d）$T_d = 0.6$ ms, $K_{pi} = 20$ without the voltage feedforward

requirement of (6) is met. As an example with $f_c = 740$ Hz < 913 Hz and $K_{pi} = 465 < 523.5$ given by Fig. 15 (b). The simulation results given in Fig. 15 verify the correctness of (6).

Considering the voltage feedforward loop, the stability of the system requires $K_{pi}K_{pv} \leq 1$, which is indicated by (15). Fig. 16 shows the simulation results with $T_d = 0.3$ ms ,$T_{d1} = 0.1$ ms and $\omega_c = 4070$, where the unstable operation of the system when $K_{pi}K_{pv} > 1$ can be clearly observed, as shown in Fig. 16 (c), and thus, the correctness of (15) is verified.

For the condition that voltage feedforward is not adopted, either the proportional or the integral gain of the PR regulator of the voltage loop can be designed to have dominant effect at the

crossover frequency. In former case, Eq. (22), i.e., $K_{pi}K_{pv} < 1$, should be satisfied. This is verified by Fig. 17, which illustrates the unstable operation of the MMC system when $K_{pi}K_{pv} > 1$ (see Fig. 17 (c)) and the stable operation when $K_{pi}K_{pv} < 1$ (see Fig. 17 (a) and (b)). In the latter case, (24) should be met in order for the stable operation of the system, which is verified by Fig. 18.

Table II shows the simulated and calculated overshoot of the fault current with different parameters under a three phase short circuit fault with $L_g = 0.01$ H and $T_d = 0.3$ ms. From TABLE II, it can be seen that the error between simulation and the time-domain waveform of the simulated and calculated fau

TABLE II
OVERSHOOT OF FAULT CURRENT IN DIFFERNET
PARAMETERS WITH VOLTAGE FEEDFORWARD

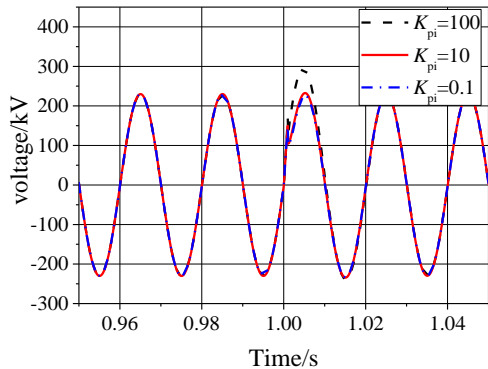| K_{pi}	I_{max}		
	simulation/p.u.	calculation/ p.u.	error/%
10	1.30	1.24	4.61
20	1.21	1.18	2.4
30	1.17	1.14	2.56
40	1.15	1.13	1.73
50	1.14	1.11	2.63
60	1.13	1.08	4.42
70	1.12	1.05	6.25

Fig. 20 The parametric impact on stiffness of the voltage

-lt current. The close match between the calculation and simulation verify the correctness of the theoretical analysis. Fig. 19(c) and (d) show the effect of the voltage feedforward on fault current with different time delay, it can be seen that the overshoot of fault current is significantly increased if the voltage feedforward is not used, which also agrees with the theoretical analysis.

Fig. 20 shows the dynamics of the output voltage of the MMC under 0.5 kA current steps. According to the section IV, the modulus of the output impendence is smallest when $K_{pi} = 0.1$ and largest when $K_{pi} = 100$. Therefore, the largest overvoltage of the MMC (about 1.3 p.u.) can be observed when $K_{pi} = 100$, while the best voltage stiffness against current variation is achieved when $K_{pi} = 0.1$. To increase the stiffness of the output voltage of the MMC, the K_{pi} should be set as small as possible within the satisfactory region.

VI. CONCLUSIONS

This paper presents a systematic parameters tuning guildline for the dual-loop voltage-controlled MMC considering the requirement of voltage stability, transient fault current limitation and stiffness of voltage against load current change. The impact of voltage feedforward on stability and fault current limitation is investigated. It is found out that the overshoot of the fault current increases significantly if the voltage feedforward is not used. Within the satisfactory region of the parameters, the smaller K_{pi} will lead to higher stiffness of the output voltage of the MMC against load current change. Based on the proposed method, the controller parameters can be calculated directly without trial and error. The effectiveness of the proposed method is verified by time domain simulation.

REFERENCES

[1] J. Khazaei, M. Beza and M. Bongiorno, "Impedance analysis of modular multi-level converters connected to weak AC grids," *IEEE Trans. Power Syst.*, vol. 33, no. 4, pp. 4015-4025, July 2018.

[2] G. Wu et al., "Analysis and design of vector control for VSC-HVDC connected to weak grids," *CSEE J. Power Energy Syst.*, vol. 3, no. 2, pp. 115-124, June 2017..

[3] Z. Bian and Z. Xu, "Fault ride-through capability enhancement strategy for VSC-HVDC systems supplying for passive industrial installations," *IEEE Trans. Power Deliv.*, vol. 31, no. 4, pp. 1673-1682, Aug. 2016..

[4] A. Moawwad, M. S. El Moursi and W. Xiao, "A novel transient control strategy for VSC-HVDC connecting offshore wind power plant," *IEEE Trans. Sustain. Energy*, vol. 5, no. 4, pp. 1056-1069, Oct. 2014.

[5] Y. Li et al., "Over-voltage suppression methods for the MMC-VSC-HVDC wind farm integration system," *IEEE Trans. Circuits Syst. II-Express Briefs.* early access, 2019.

[6] Y. Jing, R. Li, L. Xu and Y. Wang, "Enhanced AC voltage and frequency control of offshore MMC station for wind farm connection," *IET Renew. Power Gener.,* vol. 12, no. 15, pp. 1771-1777, 19 11 2018.

[7] C. Bao, X. Ruan, X. Wang, W. Li, D. Pan and K. Weng, "Step-by-step controller design for LCL-type grid-connected inverter with capacitor–current-feedback active-damping," *IEEE Trans. Power Electron.*, vol. 29, no. 3, pp. 1239-1253, March 2014..

[8] L. Wang and N. Ertugrul, "Selection of PI compensator parameters for VSC-HVDC system using decoupled control strategy," *2010 20th Australasian Universities Power Engineering Conference*, Christchurch, 2010, pp. 1-7.

[9] P. C. Loh and D. G. Holmes, "Analysis of multiloop control strategies for LC/CL/LCL-filtered voltage-source and current-source inverters," *IEEE Trans. Ind. Appl.*, vol. 41, no. 2, pp. 644-654, March-April 2005.

[10] Y. W. Li, "Control and resonance damping of voltage-source and current-source converters with LC filters," *IEEE Trans. Ind. Appl.*, vol. 56, no. 5, pp. 1511-1521, May 2009.

[11] X. Wang, P. C. Loh and F. Blaabjerg, "Stability analysis and controller synthesis for single-loop voltage-controlled VSIs," *IEEE Trans. Power Electron.*, vol. 32, no. 9, pp. 7394-7404, Sept. 2017.

[12] J. Lyu, X. Cai and M. Molinas, "Optimal design of controller parameters for improving the stability of MMC-HVDC for wind farm integration," *IEEE J. Emerg. Sel. Top. Power Electron.,* vol. 6, no. 1, pp. 40-53, March 2018..

[13] W. Xiang, S. Yang, L. Xu, J. Zhang, W. Lin and J. Wen, "A transient voltage-based DC fault line protection scheme for MMC-based DC grid embedding DC breakers," *IEEE Trans. Power Deliv.*, vol. 34, no. 1, pp. 334-345, Feb. 2019.

[14] X. Pei, H. Pang, Y. Li, L. Chen, X. Ding and G. Tang, "A novel ultra-high-speed traveling-wave protection principle for VSC-based DC grids," *IEEE Access*, vol. 7, pp. 119765-119773, 2019.

[15] M, Guan et al. "Modeling and control of modular multilevel converter based VSC-HVDC system connected to passive networks". *CES Trans. Elect.*, 2013, 28(2): 255-263.

[16] U. Karaagac, J. Mahseredjian, L. Cai and H. Saad, "Offshore wind farm modeling accuracy and efficiency in MMC-based multiterminal HVDC connection," *IEEE Trans. Power Deliv.*, vol. 32, no. 2, pp. 617-627, April 2017.

[17] S. K. Chaudhary, R. Teodorescu, P. Rodriguez, P. C. Kjaer and A. M. Gole, "Negative sequence current control in wind power plants with VSC-HVDC connection," *IEEE Trans. Sustain. Energy*, vol. 3, no. 3, pp. 535-544, July 2012.

[18] K. Jia, R. Chen, Z. Xuan, Z. Yang, Y. Fang and T. Bi, "Fault characteristics and protection adaptability analysis in VSC-HVDC-connected offshore wind farm integration system," *IET Renew. Power Gener.*, vol. 12, no. 13, pp. 1547-1554, 1 10 2018.

[19] G. Bu, Y Li et al. "Analysis of the short-circuit current of MMC-HVDC [J]." *CSEE J. Power Energy Syst.* 37.21 (2017): 6303-6312.

[20] H. Liu and J. Sun, "Voltage stability and control of offshore wind farms with AC collection and HVDC transmission," *IEEE J. Emerg. Sel. Top. Power Electron.*, vol. 2, no. 4, pp. 1181-1189, Dec. 2014.

[21] M. Raza, E. Prieto-Araujo and O. Gomis-Bellmunt, "Small-signal stability analysis of offshore AC network having multiple VSC-HVDC systems," *IEEE Trans. Power Deliv.*, vol. 33, no. 2, pp. 830-839, April 2018.

[22] Z. Bian and Z. Xu, "Fault ride-through capability enhancement strategy for VSC-HVDC systems supplying for passive industrial installations," *IEEE Trans. Power Deliv.*, vol. 31, no. 4, pp. 1673-1682, Aug. 2016.

[23] H. Wu, "A modified grid voltage feedforward method to improve the stability-robustness of the grid-connected voltage source converter

under weak grid conditions," *2016 China International Conference on Electricity Distribution (CICED)*, Xi'an, 2016, pp. 1-5.

[24] J. Li, G. Konstantinou, H. R. Wickramasinghe and J. Pou, "Operation and control methods of modular multilevel converters in unbalanced AC grids: A Review," *IEEE J. Emerg. Sel. Top. Power Electron.*, vol. 7, no. 2, pp. 1258-1271, June 2019.

[25] Q. Yan, X. Wu, X. Yuan and Y. Geng, "An improved grid-voltage feedforward strategy for high-power three-phase grid-connected inverters based on the simplified repetitive predictor," *IEEE Trans. Power Electron*, vol. 31, no. 5, pp. 3880-3897, May 2016.

[26] X. Li, J. Fang, Y. Tang and X. Wu, "Robust design of LCL filters for single-current-loop-controlled grid-connected power converters with unit PCC voltage feedforward," *IEEE J. Emerg. Sel. Top. Power Electron.*, vol. 6, no. 1, pp. 54-72, March 2018.

[27] Y. Xiong and Y. Ye, "Physical interpretations of grid voltage full feedforward for grid-tied inverter," *IEEE Trans. Circuits Syst. II-Express Briefs,* vol. 66, no. 2, pp. 267-271, Feb. 2019.

[28] D. N. Zmood and D. G. Holmes, "Stationary frame current regulation of PWM inverters with zero steady-state error," *IEEE Trans. Power Electron.*, vol. 18, no. 3, pp. 814-822, May 2003.

[29] A. Vidal et al., "Assessment and optimization of the transient response of proportional-resonant current controllers for distributed power generation systems," *IEEE Trans. Ind. Electron.*, vol. 60, no. 4, pp. 1367-1383, April 2013.

[30] H. Wu, X. Wang and Ł. Kocewiak, "Impedance-based stability analysis of voltage-controlled MMCs feeding linear AC systems," *IEEE Trans. Ind. Electron.,* early access, 2019.

[31] A. G. Yepes, F. D. Freijedo, Ó. Lopez and J. Doval-Gandoy, "Analysis and design of resonant current controllers for voltage-source converters by means of Nyquist diagrams and sensitivity function," *IEEE Trans. Ind. Electron.*, vol. 58, no. 11, pp. 5231-5250, Nov. 2011.

[32] J. Xu, A. M. Gole and C. Zhao, "The use of averaged-value model of modular multilevel converter in DC grid," *IEEE Trans. Power Deliv.*, vol. 30, no. 2, pp. 519-528, April 2015.
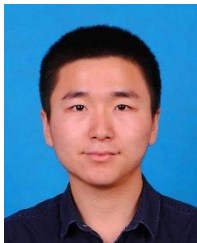
Yingbiao Li received the B.S. degree in electrical engineering from Wuhan University, Wuhan, China, in 2014, the M.S. degree from China Electric Power Research Institute, Beijing, China, in 2017. He is currently working toward the Ph.D. degree in China Electric Power Research Institute. His main research interest is transient stability analysis of the power electronic based power systems.

Jianbo Guo received the B.S. degrees from Huazhong University of Science and Technology, Wuhan, China, in 1982 and M.S. degrees from China Electric Power Research Institute, Beijing, China, in 1984.

From 2010 to 2019, he worked as Chairman of China Electric Power Research Institute. Since 2013, he has been an elected Academician of the Chinese Academy of Engineering, Beijing, China. He is currently the deputy chief engineer of State Grid Corporation of China, the vice Chairman of China Electrical Engineering Society, and the Honorary Chairman of China Electric Power Research Institute. He has been dedicated to the clean use of energy and the development of environmentally friendly power grid. He has long engaged in power system analysis & control. He has made remarkable achievements in power grid planning, improving security, reliability and transfer capability of power grid, and security of wind power integration. As the principal investigator, he participated in Chinese National Programs for Three Gorges Power Transmission Project and many other important grid planning studies. He presided over the development plan for Chinese National Grid Interconnection Project (from 2020 to 2050). He successfully developed Thyristor Controlled Series Compensation (TCSC) and UHV series compensator (1000kV) with proprietary IPR.

Prof. Guo won the first and second prizes of the National Science and Technology Progress Award in 2008 and 2015, the Ho Leung Ho Lee Foundation Science and Technology Progress Award in 2011 and FEIAP Engineer of the Year Award 2018, in 2019.
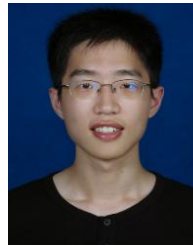
Heng Wu (S'17) received the B.S. and M.S. degrees in electrical engineering from Nanjing University of Aeronautics and Astronautics (NUAA), Nanjing, China, in 2012 and 2015, respectively. He is currently working toward the Ph.D. degree in power electronic engineering in Aalborg University, Aalborg, Denmark.

From 2015 to 2017, He was an Electrical Engineer with NR Electric Co., Ltd, Nanjing, China. He was a guest researcher with Ørsted Wind Power, Fredericia, Denmark, from November to December, 2018, and with Bundeswehr University Munich, Germany, from September to December, 2019. His research interests include the modelling and stability analysis of the power electronic based power systems.

Xiongfei Wang (S'10-M'13-SM'17) received the B.S. degree from Yanshan University, Qinhuangdao, China, in 2006, the M.S. degree from Harbin Institute of Technology, Harbin, China, in 2008, both in electrical engineering, and the Ph.D. degree in energy technology from Aalborg University, Aalborg, Denmark, in 2013.

Since 2009, he has been with the Department of Energy Technology, Aalborg University, where he became an Assistant Professor in 2014, an Associate Professor in 2016, a Professor and Research Program Leader for Electronic Power Grid (eGrid) in 2018, and the Director of Aalborg University-Huawei Energy Innovation Center in 2020. His current research interests include modeling and control of grid-interactive power converters, stability and power quality of converter-based power systems, active and passive filters.

Dr. Wang was selected into Aalborg University Strategic Talent Management Program in 2016. He has received six IEEE Prize Paper Awards, the 2016 Outstanding Reviewer Award of IEEE TRANSACTIONS ON POWER ELECTRONICS, the 2018 IEEE PELS Richard M. Bass Outstanding Young Power Electronics Engineer Award, the 2019 IEEE PELS Sustainable Energy Systems Technical Achievement Award, and the 2019 Highly Cited Researcher by Clarivate Analytics (former Thomson Reuters). He serves as a Member at Large for Administrative Committee of IEEE Power Electronics Society in 2020-2022, and an Associate Editor for the IEEE TRANSACTIONS ON POWER ELECTRONICS, the IEEE TRANSACTIONS ON INDUSTRY APPLICATIONS, and the IEEE JOURNAL OF EMERGING AND SELECTED TOPICS IN POWER ELECTRONICS.

Bing Zhao (M'11) received the B.S. and M.S. degrees from Xi'an University of Technology, Xi'an, China, in 2003 and 2006, respectively, both in electrical engineering, and the Ph.D. degree from China Electric Power Research Institute, Beijing, China, in 2009.

Since 2009, he has been with the China Electrical Power Research Institute. He is a senior engineer. His current interests involve the areas of power system analysis and control.

Shanshan Wang received the B.S. and M.S. degrees in electrical engineering from Shandong University, Ji'nan, Chain, in 2003 and 2006, respectively, and the Ph.D. degree from China Electric Power Research Institute, Beijing, China, in 2011.

From 2008 to 2020, as a core member, she participated in the scientific research and engineering solution of Shanghai Nanhui transmission system and Zhangbei ±500kV DC grid based on VSC, devoted to the research of mathematical model, control theory and topology structure on VSC transmission system, and accumulated rich scientific research and engineering experience in this field.

Guanglu Wu received the B.S. degree from North China Electric Power University, Beijing, China, in 2012 and the PhD degree from China Electric Power Research Institute, Beijing, China, in 2018, both in electrical engineering. He is currently working as an engineer in the Power System Department of China Electric Power Research Institute, Beijing, China.

His research interests include VSC-HVDC, DC grid, power converter control and stability analysis of the power system with power electronic devices.